

Magneto-optical observation of four-wave scattering in a 15-nm Ni₈₁Fe₁₉ film during large-angle magnetization precession

H. T. Nembach,^{1,*} K. L. Livesey,^{2,†} M. P. Kostylev,² P. Martin-Pimentel,³ S. J. Hermsdoerfer,³ B. Leven,³ J. Fassbender,⁴ and B. Hillebrands³

¹*Electromagnetics Division, National Institute of Standards and Technology, Boulder, Colorado 80305, USA*

²*School of Physics M013, University of Western Australia, 35 Stirling Highway, Crawley WA 6009, Australia*

³*Fachbereich Physik and Research Center OPTIMAS, Technische Universität Kaiserslautern, Erwin-Schrödinger-Strasse 56, D-67663 Kaiserslautern, Germany*

⁴*Forschungszentrum Dresden-Rossendorf e.V., Institut für Ionenstrahlphysik und Materialforschung, Bautzner Landstrasse 400, D-01328, Dresden, Germany*

(Received 27 January 2011; revised manuscript received 15 September 2011; published 14 November 2011)

Large-angle magnetization precession induced by a short pulsed magnetic field in a 15-nm thick Ni₈₁Fe₁₉ film is observed by use of a time-resolved magneto-optical Kerr effect technique with sensitivity to all three components of the magnetization vector. A reduction of the magnitude of the magnetization vector $|\mathbf{M}|$ during large-angle precession is inferred and indicates incoherent dynamics due to excitation of traveling spin waves with wavelengths smaller than the diameter of the sampling area, that is, the laser spot size for the magneto-optical measurements. The reduction in $|\mathbf{M}|$ depends on the magnetic bias field H_{bias} , which can be qualitatively understood by comparison to the theoretical threshold for observing four-magnon scattering in a small time interval t . We estimate that two-magnon scattering cannot explain the experimental results.

DOI: [10.1103/PhysRevB.84.184413](https://doi.org/10.1103/PhysRevB.84.184413)

PACS number(s): 75.40.Gb, 75.30.Ds, 75.70.-i, 76.20.+q

I. INTRODUCTION

For many years the relaxation mechanisms in magnetic materials have been studied by use of ferromagnetic resonance (FMR) experiments. In these experiments the magnetization is driven by a continuous oscillating electromagnetic field. Above a certain threshold power (or precession amplitude), intrinsic magnon-magnon interactions become an important contribution to the damping of the FMR or $k = 0$ mode. Energy is transferred from the FMR mode to traveling spin-wave modes via three- or four-wave scattering processes.

In the past decade the damped magnetization precession in thin metallic films that results after application of a short pulsed magnetic field has been studied with a variety of techniques.¹⁻⁵ Precessional magnetization reversal induced by tailored applied field pulses is significantly faster than domain wall nucleation and propagation and therefore has application to information storage.⁶⁻⁸ The large angles attainable in these experiments mean that the damping mechanisms have different relative contributions compared with FMR experiments. Intrinsic nonlinear damping is much larger than in small-angle experiments.^{9,10} In thin magnetic films and for small fields, four-wave scattering is the dominant nonlinear process.^{10,11}

Evidence that traveling spin waves are excited during magnetization precession is given by a measured reduction in the magnitude of the magnetization vector $|\mathbf{M}|$, as seen by Silva *et al.*⁵ in a Ni₈₁Fe₁₉ film by use of time-resolved magnetization-induced second-harmonic generation (SHG). This is a reduction in $|\mathbf{M}|$ due to the finite laser spot size of the optical measurement. In other words, the measurement represents a spatial average of the magnetization vector. Silva *et al.*⁵ measured the in-plane components of the magnetization vector, and the out-of-plane component was assumed small and hence was neglected. Gerrits *et al.*¹² studied large-angle magnetization dynamics in a Ni₈₀Fe₂₀ film for a range of bias field magnitudes along the easy axis and pulse field amplitudes.

They found a reduction of $|\mathbf{M}|$ for small bias fields. Details of the measurement method used to resolve the two in-plane components of the magnetization vector by SHG can be found in Refs. 13 and 14.

In this work the time evolution of all three components of the magnetization vector is measured by magneto-optical Kerr effect (MOKE) magnetometry. We employ a special measurement procedure that allows one to deconvolute the contributions of the three magnetization components to the magneto-optical signal. The spatial average of the magnetization vector's magnitude in a 15-nm thick Ni₈₁Fe₁₉ film after excitation by a pulse field is determined for different bias field strengths applied along the magnetic easy and hard axis, respectively. The experimental results are then explained qualitatively by use of an existing theory for four-wave scattering in thin films that is based on a semiclassical spin-wave Hamiltonian. The same traveling spin waves are excited via intrinsic four-wave scattering and extrinsic two-wave scattering by inhomogeneities. However, two-wave scattering cannot explain the results, since the scattering rate is far too small for a film with a reasonably small number of defects. Hence, the experimental results represent a true observation of four-wave scattering.

In Sec. II we detail the experimental technique and the results for $|\mathbf{M}|$ as a function of bias field. In Sec. III we derive the threshold for observing four-wave scattering in the Ni₈₁Fe₁₉ film in a small time interval t . The semiclassical Hamiltonian theory is summarized in the Appendix and is based on previous works.^{9,11,15} In Sec. IV we qualitatively compare the experimental and theoretical results. The conclusions are given in Sec. V.

II. MAGNETO-OPTIC EXPERIMENT

A Ni₈₁Fe₁₉ film with a thickness of 15 nm was grown on a 100- μm thick glass substrate by means of molecular beam

epitaxy in an applied field. The magnetization dynamics were measured by time-resolved MOKE magnetometry. A pulsed diode laser operating at 407 nm with a pulse width of 83 ps full width at half maximum (FWHM) was employed. The angle of light incidence was 62° and the laser beam was *s* polarized. The sample was placed film-side down on a shorted 430- μm wide microstripline, which had an impedance of 49 Ω . The laser spot was positioned at the middle of the microstrip line to ensure maximum uniformity of the pulsed magnetic field within the probe area.

For basic characterization, hysteresis curves were measured as a function of the in-plane direction of the magnetic field. The remanence values of the hysteresis curves show a uniaxial anisotropy. The anisotropy field H_{uni} of the uniaxial anisotropy was determined by two series of time-resolved measurements. For the first series, the sample was excited by a microwave field of 100 mW (20 dBm) power. The microwave frequency was varied in the range of 0.8–2 GHz in 0.1 GHz steps. For each frequency the precession amplitude was determined as a function of the applied magnetic field. This yields the resonance field for each frequency. For the second series, the magnetization was excited by a 10 V pulse and the precession frequency was determined for each applied bias magnetic field. The experimental results were then fitted with the Kittel formula under the assumption $H_{\text{appl}} \ll M_s$, which is fulfilled in the experiment

$$\omega^2 = \mu_0^2 \gamma^2 (H_{\text{appl}} + H_{\text{uni}}) M_s,$$

where H_{appl} is the applied magnetic field, H_{uni} is the unidirectional anisotropy field, M_s is the saturation magnetization, and γ is the gyromagnetic ratio. Assuming $\gamma = 1.76 \times 10^{11} \text{ s}^{-1} \text{ T}^{-1}$ ($1.76 \times 10^7 \text{ Oe}^{-1} \text{ s}^{-1}$), the averaged results from the two measurement methods are $H_{\text{uni}} = 0.61 \pm 0.02 \text{ kA m}^{-1}$ ($7.6 \pm 0.2 \text{ Oe}$) and $M_s = 867 \pm 2 \text{ kA m}^{-1}$ ($867 \pm 2 \text{ emu/cm}^3$). The difference of the results obtained by these two excitation methods are only marginal.

Different magneto-optical methods have been employed in the past to determine the components of the magnetization vector.^{16–22} Here we employed a special measurement procedure to determine the time evolution of all three components of the magnetization vector in calibrated units. Our measurement procedure is an extension of the procedure employed by Ding *et al.*²¹ to study the spin-reorientation process in ultrathin ferromagnetic films.

A MOKE measurement in longitudinal geometry depends linearly on two magnetization components: the out-of-plane (m_z) and the in-plane component (m_x) that lies in the plane of incidence of the light. In addition, there are quadratic magneto-optical Kerr effect contributions.²³ These higher-order contributions have recently been the subject of much interest.^{24,25} The Kerr rotation in longitudinal geometry is given for the 0° measurement (see Fig. 1)^{26,27} and is, assuming that the magneto-optical constants themselves are independent of the sample orientation,

$$\begin{aligned} \theta_K(\phi = 0^\circ) = & \theta_K^{\text{lon}} \cdot m_x + \theta_K^{\text{pol}} \cdot m_z + \theta_K^{\text{quad}(l,t)} \cdot m_x m_y \\ & + \theta_K^{\text{quad}(p,t)} \cdot m_z m_y + \theta_K^{\text{quad}(p,l)} \cdot m_z m_x \end{aligned}$$

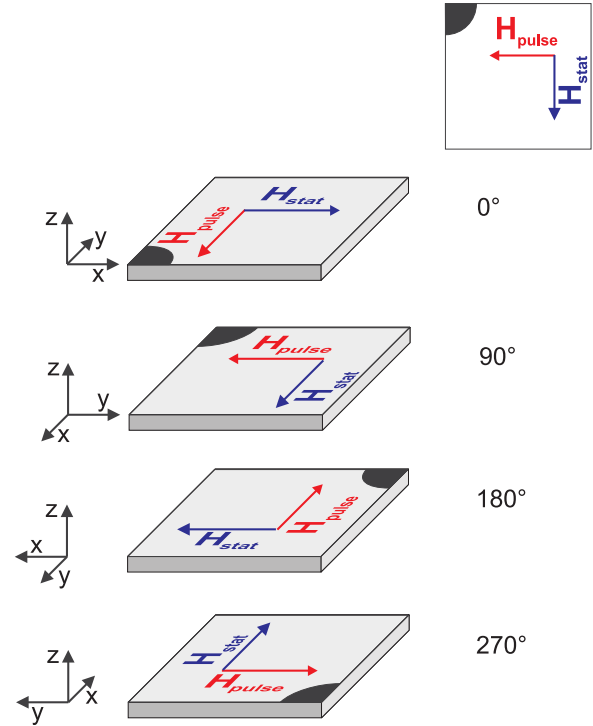


FIG. 1. (Color online) Measurement procedure to obtain time dependence of all three components of the magnetization vector. After each measurement the sample is rotated together with the applied magnetic field and the microstrip line in the fixed laser beam.

$$\begin{aligned} & + \theta_K^{\text{quad}(l^2,t^2)} \cdot (m_x^2 - m_y^2) + \theta_K^{\text{quad}(p^2,t^2)} \\ & \cdot (m_y^2 - m_z^2) + \theta_K^{\text{quad}(p^2,l^2)} \cdot (m_z^2 - m_x^2), \quad (1) \end{aligned}$$

where m_x , m_y , and m_z are the components of the normalized magnetization vector \mathbf{m} with $|\mathbf{m}| = \sqrt{m_x^2 + m_y^2 + m_z^2} = 1$. θ_K^{lon} and θ_K^{pol} are the longitudinal and polar magneto-optical constants, respectively. $\theta_K^{\text{quad}(l,t)}$, $\theta_K^{\text{quad}(p,t)}$, $\theta_K^{\text{quad}(p,l)}$, $\theta_K^{\text{quad}(l^2,t^2)}$, $\theta_K^{\text{quad}(p^2,t^2)}$, and $\theta_K^{\text{quad}(p^2,l^2)}$ are the six quadratic magneto-optical constants.

The precessional motion of the magnetization in this experiment is highly elliptical. Therefore m_z is significantly smaller than m_x and m_y . Also it will be shown that the quadratic magneto-optical constants are two orders of magnitude smaller than the polar magneto-optical constant. This allows us to neglect any quadratic magneto-optical contributions, which are proportional to either m_z or m_z^2 . The above equation then simplifies to

$$\begin{aligned} \theta_K(\phi = 0^\circ) = & \theta_K^{\text{lon}} \cdot m_x + \theta_K^{\text{pol}} \cdot m_z + \theta_K^{\text{quad}(l,t)} \cdot m_x m_y \\ & + \theta_K^{\text{quad}(l^2,t^2)} \cdot (m_x^2 - m_y^2) \\ & + \theta_K^{\text{quad}(p^2,t^2)} \cdot m_y^2 - \theta_K^{\text{quad}(p^2,l^2)} \cdot m_x^2. \quad (2) \end{aligned}$$

The longitudinal and polar magneto-optical constants for the sample were determined by measurement of in-plane and out-of-plane hysteresis curves at the same angle of incidence as the time-resolved measurements. Half of the amplitude of the respective hysteresis curves gives these two magneto-optical

constants, namely $\theta_K^{\text{pol}} = 141.8 \pm 0.9$ mdeg and $\theta_K^{\text{lon}} = 37.5 \pm 0.3$ mdeg.

In order to deconvolute the three components of the magnetization vector, a series of four measurements was performed for each bias field. The addition of one additional measurement step compared to the procedure employed by Ding *et al.*²¹ allows us to account for part of the quadratic contributions to the magneto-optical Kerr effect signal.

In Fig. 1 we show the four steps of the measurement procedure. Prior to the measurement procedure any tilt of the sample with respect to the plane of incidence is removed. Moreover, prior to each measurement it is determined with a fiducial mark that the laser is always focused onto the same area on the sample. After each measurement the sample is rotated by 90° together with the static applied magnetic field and the microstripline, which generates the dynamic magnetic field. During this rotation, only the magneto-optical geometry is changed, and so the geometry of the sample, with respect to the static and the dynamic magnetic field, remains the same. For the four measurements, the following formulas apply for the measured Kerr signal:

$$\begin{aligned} \theta_K(\phi = 0^\circ) &= \theta_K^{\text{lon}} \cdot m_x + \theta_K^{\text{pol}} \cdot m_z + \theta_K^{\text{quad}(1,t)} \cdot m_x m_y \\ &\quad + \theta_K^{\text{quad}(l^2,t^2)} \cdot (m_x^2 - m_y^2) + \theta_K^{\text{quad}(p^2,t^2)} \\ &\quad \cdot m_y^2 - \theta_K^{\text{quad}(p^2,l^2)} \cdot m_x^2, \end{aligned} \quad (3)$$

$$\begin{aligned} \theta_K(\phi = 90^\circ) &= \theta_K^{\text{lon}} \cdot m_y + \theta_K^{\text{pol}} \cdot m_z - \theta_K^{\text{quad}(1,t)} \cdot m_x m_y \\ &\quad + \theta_K^{\text{quad}(l^2,t^2)} \cdot (m_y^2 - m_x^2) \\ &\quad + \theta_K^{\text{quad}(p^2,t^2)} \cdot m_x^2 - \theta_K^{\text{quad}(p^2,l^2)} \cdot m_y^2, \end{aligned} \quad (4)$$

$$\begin{aligned} \theta_K(\phi = 180^\circ) &= -\theta_K^{\text{lon}} \cdot m_x + \theta_K^{\text{pol}} \cdot m_z + \theta_K^{\text{quad}(1,t)} \cdot m_x m_y \\ &\quad + \theta_K^{\text{quad}(l^2,t^2)} \cdot (m_x^2 - m_y^2) \\ &\quad + \theta_K^{\text{quad}(p^2,t^2)} \cdot m_y^2 - \theta_K^{\text{quad}(p^2,l^2)} \cdot m_x^2, \end{aligned} \quad (5)$$

$$\begin{aligned} \theta_K(\phi = 270^\circ) &= -\theta_K^{\text{lon}} \cdot m_y + \theta_K^{\text{pol}} \cdot m_z - \theta_K^{\text{quad}(1,t)} \cdot m_x m_y \\ &\quad + \theta_K^{\text{quad}(l^2,t^2)} \cdot (m_y^2 - m_x^2) \\ &\quad + \theta_K^{\text{quad}(p^2,t^2)} \cdot m_x^2 - \theta_K^{\text{quad}(p^2,l^2)} \cdot m_y^2. \end{aligned} \quad (6)$$

These four simultaneous equations then yield:

$$\frac{\theta_K(0^\circ) - \theta_K(180^\circ)}{2} = \theta_K^{\text{lon}} \cdot m_x, \quad (7)$$

$$\frac{\theta_K(90^\circ) - \theta_K(270^\circ)}{2} = \theta_K^{\text{lon}} \cdot m_y, \quad (8)$$

$$\begin{aligned} &\frac{\theta_K(0^\circ) - \theta_K(90^\circ) + \theta_K(180^\circ) - \theta_K(270^\circ)}{4} \\ &= \theta_K^{\text{quad}(1,t)} m_x m_y + X_K^{\text{quad}} (m_x^2 - m_y^2), \end{aligned} \quad (9)$$

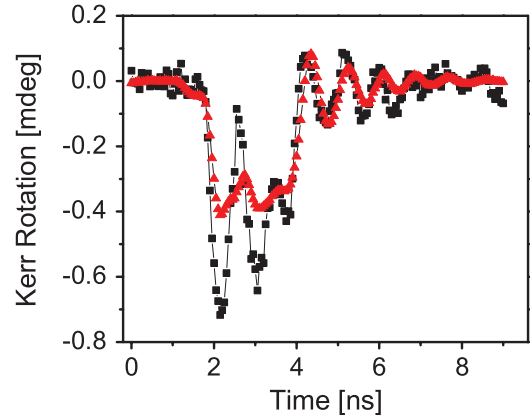


FIG. 2. (Color online) Comparison of the left- and right-hand side of Eq. (9). The left-hand side is the higher-order magneto-optical contribution to the Kerr signal, which is determined by the four measurements, and is arbitrarily set to zero before the pulse onset (black squares). The red triangles show the best fit of the right-hand side of Eq. (9), given that we know m_x and m_y , and this fit corresponds to $\theta_K^{\text{quad}(1,t)} = 1.6 \pm 0.3$ mdeg and $X_K^{\text{quad}} = -0.6 \pm 0.8$ mdeg. For those fits a time independent offset was added, which sets the magneto-optical signal for $t = 0$ ns to zero. The magnetic field $H_{\text{bias}} = 0.61$ kA m⁻¹ (7.6 Oe) is applied parallel to the easy axis.

$$\begin{aligned} &\frac{\theta_K(0^\circ) + \theta_K(90^\circ) + \theta_K(180^\circ) + \theta_K(270^\circ)}{4} \\ &= \theta_K^{\text{pol}} \cdot m_z + \frac{1}{2} \theta_K^{\text{quad}(p^2,l^2)} \cdot (m_x^2 + m_y^2) \\ &\quad + \frac{1}{2} \theta_K^{\text{quad}(p^2,t^2)} \cdot (m_x^2 + m_y^2), \end{aligned} \quad (10)$$

where $X_K^{\text{quad}} = \theta_K^{\text{quad}(l^2,t^2)} - \frac{1}{2} \theta_K^{\text{quad}(l^2,p^2)} - \frac{1}{2} \theta_K^{\text{quad}(p^2,l^2)}$ is a combination of quadratic magneto-optical constants. Equations (7) and (8) show that the two in-plane components of the magnetization vector can be extracted from the four measurements. Once m_x and m_y are known as a function of time, Eq. (9) can then be used to calculate the two constants $\theta_K^{\text{quad}(1,t)}$ and X_K^{quad} . Fits to the data for the bias magnetic field parallel to the easy axis (see Fig. 2) yield the following average values for the quadratic magneto-optical constants: $\theta_K^{\text{quad}(1,t)} = 1.6 \pm 0.3$ mdeg and $X_K^{\text{quad}} = -0.6 \pm 0.8$ mdeg. For these fits a time independent offset was added, which sets the magneto-optical signal for $t = 0$ ns to zero.

$\theta_K^{\text{quad}(1,t)}$ is between one and two orders of magnitude smaller than the linear Kerr constants $\theta_K^{\text{pol}} = 141.8 \pm 0.9$ mdeg and $\theta_K^{\text{lon}} = 37.5 \pm 0.3$ mdeg quoted above. This may be partly because the film is polycrystalline. The fact that $\theta_K^{\text{quad}(1,t)}$ is very small underlines that it was justified to drop the higher order magneto-optical contributions proportional to m_z and m_z^2 in the step from Eq. (1) to Eq. (2). We can also, therefore, assume that the remaining magneto-optical constants are small ($\theta_K^{\text{quad}(p^2,l^2)}$, $\theta_K^{\text{quad}(p^2,t^2)} \sim 0$). The quadratic magneto-optical contributions in Eq. (10) are proportional to $m_x^2 + m_y^2$. The time-dependent contribution of $m_x^2 + m_y^2$ is much smaller than 1. This together with the fact that the higher order magneto-optical constants are themselves small allows one to ignore the higher order

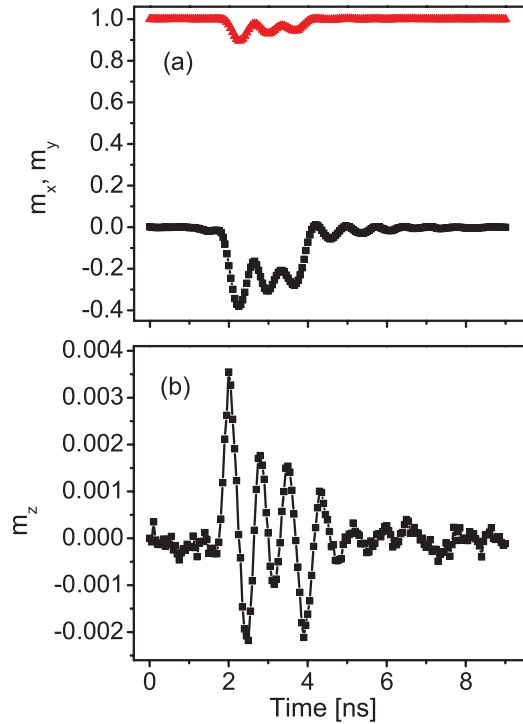


FIG. 3. (Color online) In the upper panel (a) the time evolution of the calibrated in-plane components m_x (red triangles) and m_y (black squares) are shown. The calibrated out-of-plane component m_z is shown in the lower panel (b). The magnetic field $H_{\text{bias}} = 1.07 \text{ kA m}^{-1}$ (13.5 Oe) is applied parallel to the easy axis.

magneto-optical contributions in Eq. (10) and then the out-of-plane component of the magnetization vector m_z can also be found.

To explore the dynamics during large angle precession, the magnetization is excited by a voltage pulse with an amplitude of 28.4 V, a rise time of 240 ps, and a width of 2.14 ns FWHM, which gives an effective pulse magnetic field H_{pulse} perpendicular to the bias field H_{bias} , as illustrated in Fig. 1. The magnetization trajectory can be reconstructed with the methods discussed above. In Fig. 3 the time evolution of the three calibrated magnetization components is shown for a static magnetic field $H_{\text{bias}} = 1.07 \text{ kA m}^{-1}$ (13.5 Oe) parallel to the easy axis. The normalized magnitude $|\mathbf{m}|$ of the magnetization vector and the in-plane angle of the magnetisation ϕ relative to its starting direction can be calculated from the individual components. The results for a bias field of $H_{\text{bias}} = 2.08 \text{ kA m}^{-1}$ (26.1 Oe) applied parallel to the hard axis are shown in Fig. 4. The pulse field is applied at $t \sim 1.5 \text{ ns}$ and causes the magnetization to reorient in-plane by roughly 25° , precessing about the new equilibrium direction. This reorientation implies that the field pulse has an amplitude of $H_{\text{pulse}} = 0.47 \text{ kA m}^{-1}$ (5.9 Oe).

What is most interesting is that $|\mathbf{m}|$ shows a marked reduction during the large-angle precession of between 5% and 10% in Fig. 4 (see black squares, at top).

The overlying oscillations in $|\mathbf{m}|$ are due to a slightly imperfect deconvolution of the three components of the magnetization vector. If the magnetization precession were perfectly coherent, then $|\mathbf{m}| = 1$ would hold at all times.

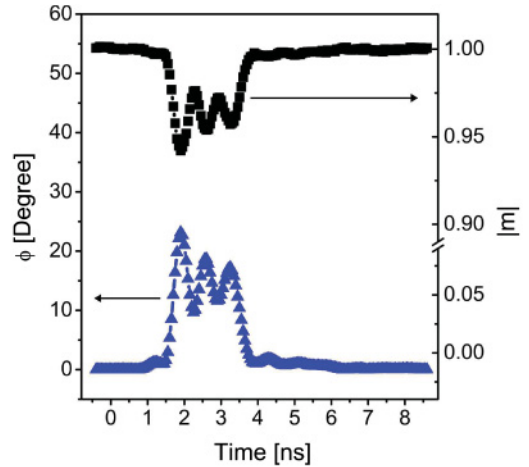


FIG. 4. (Color online) Magnetization dynamics induced by a pulse field applied at 90° to the bias field. $H_{\text{bias}} = 2.08 \text{ kA m}^{-1}$ (26.1 Oe) parallel to the hard anisotropy axis and $H_{\text{pulse}} \sim 0.47 \text{ kA m}^{-1}$ (5.9 Oe). The in-plane angle of the magnetization ϕ relative to the hard axis is shown by the blue triangles. The black squares show the magnetization vector length $|\mathbf{m}|$ as a function of time.

Instead, the reduction of the magnitude of the magnetization vector indicates the excitation of spin waves with wavelengths shorter than the diameter of the laser spot used to make the MOKE measurements.⁵ The laser spot in these experiments is an ellipse with axes of 28 and 42 μm . This means that the existence of spin waves with wave vectors $k > 1.1 \times 10^5 \text{ m}^{-1}$ may reduce the measured $|\mathbf{m}|$. Any spin waves that could be excited directly by the microstrip line would have a wave vector $k < 6500 \text{ m}^{-1}$. Therefore any spin waves contributing to a measured reduction in $|\mathbf{m}|$ must have been excited by a secondary process. These secondary processes represent extrinsic (in the case of two-magnon scattering by impurities) and/or intrinsic (in the case of three- or four-magnon scattering) damping mechanisms.

To gain further insight into the underlying damping mechanisms of the magnetization dynamics, additional measurements were carried out for a range of applied magnetic fields parallel to the easy and to the hard anisotropy direction. In Fig. 5 the reduction in $|\mathbf{m}|$, when the magnetization is at its maximum excursion angle with respect to the bias field direction, is shown for different bias fields. The length of the error bars is given by the difference of the magnitude of the magnetization vector between its first maximum and minimum during its temporal evolution for the respective bias field.

There are two key results. First, there is a much larger decrease in $|\mathbf{m}|$ for hard-axis biasing than for easy-axis biasing. This is consistent with the results of Silva *et al.*⁵ Second, for larger bias fields there is a smaller decrease in $|\mathbf{m}|$, indicating that fewer spin waves are excited. The second half of this paper is concerned with showing how four-magnon scattering of the large-angle precession may account for these results.

III. FOUR-WAVE SCATTERING THRESHOLD

In this section we outline a semiclassical, perturbative spin-wave theory to calculate the threshold for four-wave

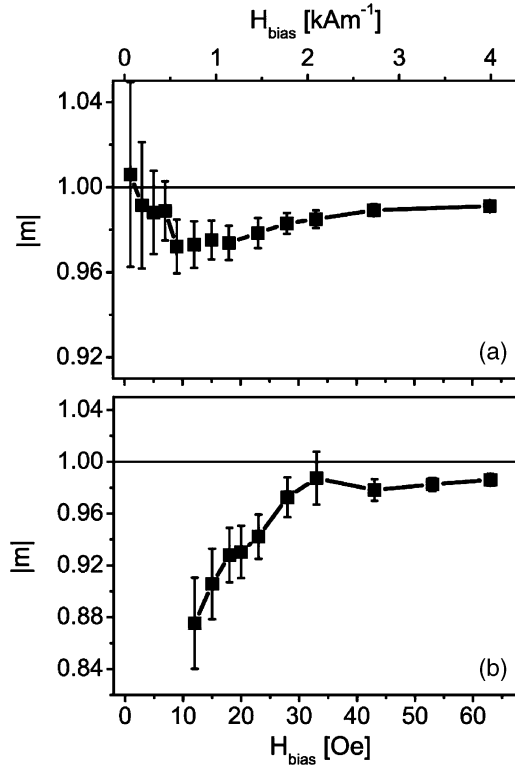


FIG. 5. The reduction in $|m|$, when the magnetization is at its maximum excursion angle with respect to the bias field direction, is shown as a function of the bias field for (a) easy-axis bias and (b) hard-axis bias.

scattering of the uniform mode to create spin waves with wavelengths smaller than the MOKE laser spot size. The full three dimensional (3D) theory of Ref. 11 is not needed here for the case of such a thin 15-nm Permalloy film, and instead we will use a 2D theory. Hence many of the expressions in Ref. 11 are greatly simplified and we provide them for the reader in the Appendix. The method is very similar to that of Dobin and Victora.⁹

We consider a perfect film with no defects. The energy of the film can be written as an integral over the film's area

$$E = L \int_A d^2\mathbf{r} W(\mathbf{r}), \quad (11)$$

where $L = 15$ nm is the film thickness and $W(\mathbf{r})$ is the energy density at position \mathbf{r} given by

$$W(\mathbf{r}) = -\frac{1}{2} \mathbf{M}(\mathbf{r}) \cdot \mathbf{h}_{\text{dip}}(\mathbf{r}) + \alpha \frac{\partial M_\mu}{\partial x_\nu} \frac{\partial M_\mu}{\partial x_\nu} - \frac{H_{\text{uni}}}{M_0} [\mathbf{M}(\mathbf{r}) \cdot \mathbf{n}]^2 - \mathbf{M}(\mathbf{r}) \cdot (\mathbf{H}_{\text{bias}} + \mathbf{H}_{\text{pulse}}). \quad (12)$$

Here the exchange constant is assumed to be $\alpha = A/(2\pi M^2)$ with $A = 10^{-11}$ J m⁻¹, H_{uni} is the effective anisotropy field equal to 0.63 kA m⁻¹ (7.9 Oe), \mathbf{n} is a unit vector in the direction of the uniaxial anisotropy axis, and the Zeeman energy includes contributions from both the bias field and the pulse field.

The dipolar field felt at position \mathbf{r} is denoted by \mathbf{h}_{dip} and is found by solving Maxwell's equations by use of a Green's function method for the 2D film geometry. It is given by

$$\mathbf{h}_{\text{dip}}(\mathbf{R}) = -\frac{4\pi}{A} \int_{A'} d^2\mathbf{R}' \sum_{\mathbf{k}} \hat{G}(\mathbf{k}) \mathbf{M}(\mathbf{R}') e^{i\mathbf{k} \cdot (\mathbf{R} - \mathbf{R}')}, \quad (13)$$

where A is the area of the film's surface and \mathbf{k} , \mathbf{R} , and \mathbf{R}' are 2D wave and position vectors in the plane of the film. The tensorial Green's function for the dipolar field is given by

$$\begin{aligned} \hat{G}(\mathbf{k}) &= \hat{G}(k, \psi) \\ &= \begin{pmatrix} P(k) \sin^2 \psi & 0 & \frac{1}{2} P(k) \sin(2\psi) \\ 0 & 1 - P(k) & 0 \\ \frac{1}{2} P(k) \sin(2\psi) & 0 & P(k) \cos^2 \psi \end{pmatrix}, \end{aligned} \quad (14)$$

where the z axis is made to coincide with the equilibrium magnetization direction and the y axis is perpendicular to the film plane. ψ is the angle of propagation of the spin-wave \mathbf{k} , measured relative to the z axis or, equivalently, relative to the internal field direction when the pulse field is applied. Also, the dipolar function $P(k) = 1 - \frac{1 - e^{-kL}}{kL}$ (Ref. 28) depends only on the magnitude of the spin-wave vector \mathbf{k} and the thickness of the film L .

The energy [Eq. (11)] is transformed into a Hamiltonian containing two-, three- and four-wave interactions by means of methods shown in the Appendix. The final form is

$$\begin{aligned} \mathcal{H} &= \sum_{\mathbf{k}} \omega_{\mathbf{k}} b_{\mathbf{k}}^* b_{\mathbf{k}} + \frac{1}{3} \sum_{1,2,3} U_{\mathbf{k}_1, \mathbf{k}_2, \mathbf{k}_3}^{(3)} \delta(\mathbf{k}_1 + \mathbf{k}_2 + \mathbf{k}_3) \\ &\quad \times [b_{\mathbf{k}_1} b_{\mathbf{k}_2} b_{\mathbf{k}_3} + \text{c.c.}] + \sum_{1,2,3} U_{\mathbf{k}_1, \mathbf{k}_2, \mathbf{k}_3}^{(1)} \delta(\mathbf{k}_1 + \mathbf{k}_2 - \mathbf{k}_3) \\ &\quad \times [b_{\mathbf{k}_1}^* b_{\mathbf{k}_2}^* b_{\mathbf{k}_3} + \text{c.c.}] + \sum_{1,2,3,4} V_{\mathbf{k}_1, \mathbf{k}_2, \mathbf{k}_3, \mathbf{k}_4}^{(1)} \\ &\quad \times \delta(\mathbf{k}_1 - \mathbf{k}_2 - \mathbf{k}_3 - \mathbf{k}_4) [b_{\mathbf{k}_1}^* b_{\mathbf{k}_2} b_{\mathbf{k}_3} b_{\mathbf{k}_4} + \text{c.c.}] \\ &\quad + \frac{1}{2} \sum_{1,2,3,4} V_{\mathbf{k}_1, \mathbf{k}_2, \mathbf{k}_3, \mathbf{k}_4}^{(2)} \delta(\mathbf{k}_1 + \mathbf{k}_2 - \mathbf{k}_3 - \mathbf{k}_4) b_{\mathbf{k}_1}^* b_{\mathbf{k}_2}^* b_{\mathbf{k}_3} b_{\mathbf{k}_4} \\ &\quad + \frac{1}{4} \sum_{1,2,3,4} V_{\mathbf{k}_1, \mathbf{k}_2, \mathbf{k}_3, \mathbf{k}_4}^{(4)} \delta(\mathbf{k}_1 + \mathbf{k}_2 + \mathbf{k}_3 + \mathbf{k}_4) \\ &\quad \times [b_{\mathbf{k}_1} b_{\mathbf{k}_2} b_{\mathbf{k}_3} b_{\mathbf{k}_4} + \text{c.c.}] + \dots, \end{aligned} \quad (15)$$

where the variable $b_{\mathbf{k}}^*$ and $b_{\mathbf{k}}$ are elliptical spin-wave variables, c.c. represents the complex conjugate, and the coefficients give the strength of interaction between different spin waves. Higher order interactions are neglected.

The two-wave coefficient provides the theoretical dispersion relation for the thin film, and this in turn provides information on exactly which nonlinear interactions will be resonant in the system and which spin waves can be excited by the uniform precession. In Fig. 6 we plot the theoretical spin-wave band for the film with a bias field of 1.35 kA m⁻¹ (17.0 Oe) applied along the hard direction. What can be seen is that the bottom of the spin-wave band is very shallow, and this means that there are no spin waves with frequency $\omega_{\mathbf{k}}$ at half the uniform precession frequency ω_0 . This in turn means that three-wave decay of the precession $\mathbf{k} = 0$ mode

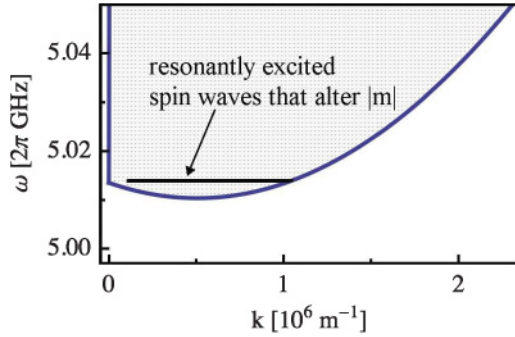


FIG. 6. (Color online) The spin-wave band (shaded) for the $\text{Ni}_{81}\text{Fe}_{19}$ film with a bias field of 1.35 kA m^{-1} (17.0 Oe) applied along the hard anisotropy direction. The horizontal black line represents all spin waves that may be resonantly excited by four-wave scattering of the $k = 0$ mode and that may alter the measurement of $|\mathbf{m}|$ ($k > 1.1 \times 10^5 \text{ m}^{-1}$).

is nonresonant in the system, and that it is four-wave decay which results in an excitation of traveling spin-wave modes (for a discussion, see Ref. 29 or 11). In Fig. 6 the spin waves that may be resonantly excited via four-wave scattering of the uniform mode and that contribute to a reduction in $|\mathbf{m}|$ ($k > 1.1 \times 10^5 \text{ m}^{-1}$) are illustrated by a horizontal line.

We now write the Hamiltonian equation of motion for a spin-wave amplitude b_k that we expect to be resonantly excited. The approximate equation of motion is given by

$$\frac{\partial b_k}{\partial t} = -i \frac{\delta \mathcal{H}}{\delta b_{-k}^*} \quad (16)$$

$$\sim -(i\omega_k + \eta_k)b_k - iV_{0,0,k,-k}^{(2)}b_0b_k^*, \quad (17)$$

where a damping constant $\eta_k = \alpha_G \gamma (H_{\text{total}} + 2\pi M_s)$ (α_G is the Gilbert damping constant and H_{total} is the total of the applied and uniaxial anisotropy fields) has been added phenomenologically into the equation as a complex part of the frequency.³⁰

Equation (17) is an approximation of Eq. (16), since the sum over all possible four-wave scattering processes has been replaced by only one scattering term, which corresponds to the scattering of two precession modes into two spin waves of equal energy but with finite momentum \mathbf{k} and $-\mathbf{k}$. Other nonlinear terms, such as those that result in such interesting effects as nonlinear frequency shift and nonlinear damping, are ignored since only terms proportional to $|b_0|^2$ are kept. This is a good approximation to make for small time scales when the system has just gone above threshold because we assume that the only mode of appreciable amplitude, straight after the pulse is applied, is the spatially uniform precession. All other spin waves with wave vectors \mathbf{k} are assumed to be at thermal levels. However, Dobin and Victora's numerical calculation showed that for a 2D Fe film the traveling spin-wave amplitudes become comparable to the uniform mode's amplitude after only 0.5 ns (Ref. 9) and then the analytic theory breaks down. Schlömann showed that including more processes within an analytic theory is difficult.³¹ Methods, such as S theory, exist for dealing with the turbulent processes far above threshold but only in steady-state limits and for continuous pumping of the system.^{29,32} We certainly do not

have a steady-state situation for the time duration of the pulse when the magnetization precession angle changes drastically over 2 ns. An analytic calculation of the reduction in $|\mathbf{m}|$ seems to be impossible, but we can still calculate the threshold for four-wave scattering in order to qualitatively explain the experimental results shown in Fig. 5.

The equation of motion [Eq. (17)] can be solved by considering that b_k is a perturbation of its linear solution which varies as $e^{-i\omega_k t}$, namely

$$b_k(t) = B_k e^{\Gamma_k(t)t} e^{-i\omega t}. \quad (18)$$

The incremental rate of increase/decrease of the spin-wave amplitude is found by substituting Eq. (18) into Eq. (17):

$$\Gamma_k(t) = |V_{0,0,k,-k}^{(2)}| |B_0|^2(t) - \eta_k. \quad (19)$$

The condition for the exponential increase in spin-wave amplitude b_k is that this incremental rate is positive. This defines the threshold uniform precession amplitude for the excitation of spin waves with wave vector \mathbf{k} ^{15,33}:

$$|B_0|^2 > \frac{\eta_k}{|V_{0,0,k,-k}^{(2)}|}. \quad (20)$$

For continuous pump experiments, this threshold may be given in terms of the rf field's power, rather than in terms of the amplitude of precession. What is perhaps more useful in these large-angle experiments is to give the threshold in terms of precession angles. However, the precession is highly elliptical for such thin films, so we write two threshold angles, corresponding to the out-of-plane angle (−) and to the in-plane angle (+) during precession that occur precisely at threshold. The result from Ref. 11 is

$$\phi_k^\pm > 2 \arcsin \left[\sqrt{\frac{\eta_k \gamma}{2M_0 |V_{0,0,k,-k}^{(2)}|}} |u_0 \pm v_0| \right], \quad (21)$$

where u_0 and v_0 are the Bogoliubov transformation coefficients [Eq. (A14)].

However, Livesey *et al.* in Ref. 11 pointed out that precession must be far above threshold to measure a detectable change in $|\mathbf{m}|$ for short time scales t . An effective threshold to measure a change in $|\mathbf{m}|$ in time t is given by

$$\phi_k^\pm(t) \gtrsim 2 \arcsin \left[\sqrt{\frac{\gamma \ln |a_{\text{therm}}|}{2t M_0 |V_{0,0,k,-k}^{(2)}|}} |u_0 \pm v_0| \right], \quad (22)$$

where $|a_{\text{therm}}|$ is the thermal spin-wave amplitude at room temperature for frequencies in the gigahertz regime and is on the order of $\sqrt{(k_B T)/\omega} \sim \sqrt{10^{-22} \text{ erg s}}$. By averaging over one precession period, the effective threshold can be written as an average angle

$$\phi_k^{av}(t) \gtrsim 2 \arcsin \left[\sqrt{\frac{\gamma (u_0^2 + v_0^2) \ln |a_{\text{therm}}|}{2t M_0 |V_{0,0,k,-k}^{(2)}|}} \right]. \quad (23)$$

Notice that the damping constant η does not enter into this equation for the effective threshold to measure a change in $|\mathbf{m}|$ in a time t .

IV. RESULTS AND DISCUSSION

The calculated four-wave scattering thresholds can be used to explain the experimental results for the behavior of $|m|$ versus bias field (Fig. 5). In Fig. 7(a) the in-plane effective threshold angle [Eq. (22)] is plotted as a function of bias field magnitude for both easy-axis biasing (solid line) and hard-axis biasing (dashed line). First, the calculated in-plane threshold angles are smaller than those seen in the experiment, indicating that four-wave scattering is possible. For example, for $H_{\text{bias}} = 2.08 \text{ kA m}^{-1}$ (26.1 Oe) in the hard direction, the in-plane threshold angle (which is the maximum angle during elliptical precession) is 9° , which is smaller than the experimental angles seen (see Fig. 4). Second, the hard-axis biasing shows a much lower threshold than the easy-axis biasing. This can explain the fact that more spin waves are excited and a greater reduction in $|m|$ is seen for hard-axis biasing than for easy-axis biasing (see Fig. 5). Third, the threshold increases with bias field, which is consistent with a smaller reduction in $|m|$ measured during precession for larger bias field, again as seen in Fig. 5. Note that there is a minimum in the threshold for hard-axis biasing at $H_{\text{bias}} \sim 1.19 \text{ kA m}^{-1}$ (15 Oe) since the magnitude of the total effective field $H_{\text{bias}} + H_{\text{pulse}} + H_{\text{uni}}$ is at a minimum here. This minimum is not evident in the experimental results [Fig. 5(b)] but this is presumably because data are only collected for hard-axis biasing with $H_{\text{bias}} > 1 \text{ kA m}^{-1}$ and therefore if the minimum is slightly lower than predicted, it

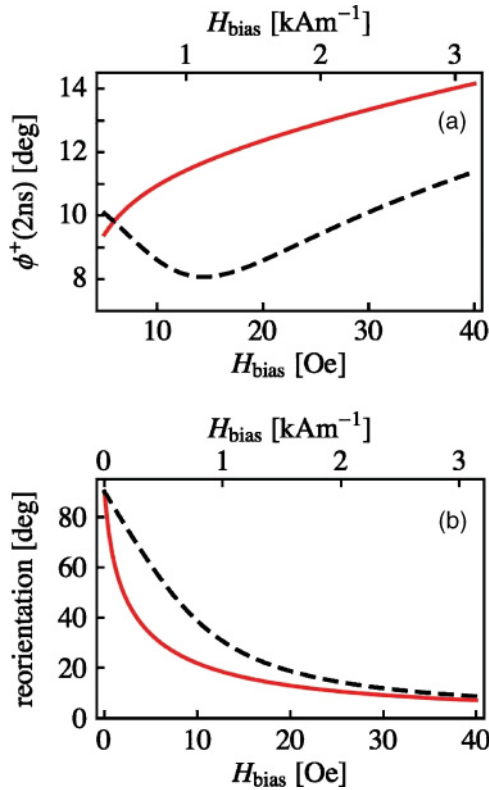


FIG. 7. (Color online) (a) The in-plane threshold angle [Eq. (22)] required to see a reduction in $|m|$ during 2 ns and (b) the reorientation angle of the magnetization due to the pulse field, both as a function of bias field strength. For biasing along the easy anisotropy axis, the results are given by a solid line (red online) and for hard-axis biasing, the results are given by a dashed line.

cannot be seen. The bias fields used must be this large in order to ensure that the magnetization is fully saturated before and after the pulse field is applied.

This is not the whole story, however, since the supercriticality of the system (how far above threshold it is) also determines the degree of nonlinearity and the relative decrease in $|m|$. In Fig. 7(b) the reorientation angle of the magnetization vector due to the pulse field is shown as a function of bias field for both easy-axis biasing (solid line) and hard-axis biasing (dashed line). This gives a rough indication of the maximum precession angles that are attainable in the experiment. For the hard-axis biasing there is a larger switching angle and thus a higher level of supercriticality, so we can argue again that there should be a larger decrease in $|m|$ compared to the case of easy-axis biasing.

Qualitatively, four-wave scattering can account for the experimental measurement of $|m|$ as a function of field H_{bias} . But, can two-wave scattering also explain the experimental results? The same spin waves, those degenerate with the FMR modes, are excited via both processes. A simple estimate of the two-wave scattering rate in $\text{Ni}_{81}\text{Fe}_{19}$ films from experiment is described below and indicates that two-wave scattering cannot cause the observed reduction in $|m|$ in such short time scales.

The field-swept ferromagnetic resonance linewidth ΔH can be related to a frequency-dependent Gilbert damping contribution together with a constant inhomogeneous broadening ΔH_0 according to $\Delta H = \Delta H_0 + \kappa\omega$, where κ is the slope of the fit.^{34,35} The inhomogeneous broadening gives an estimate of the two-magnon scattering rate by multiplying by the gyromagnetic ratio $\gamma = 1.76 \times 10^{11} \text{ s}^{-1} \text{ T}^{-1}$ ($1.76 \times 10^7 \text{ rad Oe}^{-1} \text{ s}^{-1}$). In large-angle experiments, this scattering rate does not change from the small-angle value, because the structural and magnetic inhomogeneities do not change (however, there is a larger number of excited magnons that may scatter, and so a larger change in the dynamics is seen). Thus it is justifiable to use FMR linewidth to estimate the two-magnon scattering rate in large-angle experiments and to compare this to the four-wave scattering rate.

For a 50-nm thick sputtered $\text{Ni}_{80}\text{Fe}_{20}$ film, $\Delta H_0 \sim 0.2 \text{ kA/m} \sim 2.5 \text{ Oe}$ (Ref. 36) giving a damping rate of

$$\Gamma_{2m} = (2\pi)^{-1} \gamma \Delta H_0 \sim 7 \times 10^6 \text{ s}^{-1}. \quad (24)$$

This can be considered as an upper estimate, because the film studied in our work is epitaxially deposited, rather than sputtered, and so presumably contains less inhomogeneities. Also, our 15-nm thick film is thinner and the trend is for a smaller two-magnon scattering rate for thinner films.³⁶ The corresponding decay time is on the order of 100 ns, which is much longer than the time scale of precessional switching (see, for example, Fig. 4).

The four-magnon scattering rate can be calculated with Eq. (19). The elliptical spin-wave amplitude $|B_0|^2$ at the start of the large-angle switching process first needs to be known. It can be determined by use of the Bogoliubov coefficients and the maximum in-plane magnetization precession angle ϕ_{max}

according to¹¹

$$|B_0|^2 = \frac{2M_0 \sin^2\left(\frac{\phi_{\max}}{2}\right)}{\gamma(u_0^2 + v_0^2 + 2u_0v_0)}. \quad (25)$$

By means of Fig. 4, which shows the dynamics for hard-axis biasing with $H_{\text{bias}} = 2.08 \text{ kA m}^{-1}$, we estimate $\phi_{\max} \sim 10^\circ$. By use of Eqs. (19), (25), and (A18), the four-magnon scattering rate is $\Gamma_{4m} \sim 4 \times 10^9 \text{ s}^{-1}$. This corresponds to a decay time of approximately 0.25 ns, and so it is in agreement with the subnanosecond damping seen in Fig. 4.

V. CONCLUSION

We have measured all three components of the magnetization as a function of time during magnetic field-induced precession lasting a few nanoseconds. During this precession, an apparent reduction of the magnetization vector length $|\mathbf{M}|$ is measured, indicating the secondary excitation of traveling spin waves with wavelengths smaller than the laser spot size. We have shown that four-wave scattering, and not two-wave scattering by impurities or inhomogeneities, accounts for the experimental trends for $|\mathbf{M}|$ as a function of bias field and the strong nonlinearity on such small time scales. Note also that, although the uniaxial anisotropy energy is small in the $\text{Ni}_{81}\text{Fe}_{19}$ film, the direction of biasing can dramatically change the switching dynamics when small applied fields are used.

ACKNOWLEDGMENTS

K.L.L. acknowledges the Hackett Student Fund and Seagate Technologies for support. K.L.L. and M.P.K. acknowledge support from the Australian Research Council and the University of Western Australia. The authors also wish to thank K. Postava and J. Hamrle for valuable contributions with respect to the quadratic contributions to the MO signal and H. Schultheiss for support with the experiment.

APPENDIX: CLASSICAL HAMILTONIAN FORMALISM FOR 2D FILMS

Here we present the classical spin-wave theory for a very thin (2D) magnetic film. As mentioned in the main text, the expressions are simplified compared to those contained in Ref. 11, where a full 3D theory is given.

We start with the energy of the thin magnetic film, expressed in Eq. (11), and we perform the classical analog of a 2D Holstein-Primakoff transformation to transform from magnetization to spin-wave variables. This transformation is given by

$$\begin{aligned} M^+(\mathbf{R}) &= M_x + iM_y \\ &= \sqrt{2\gamma M_0} a(\mathbf{R}) \sqrt{1 - \frac{\gamma}{2M_0} a^*(\mathbf{R})a(\mathbf{R})}, \end{aligned} \quad (A1)$$

$$M^-(\mathbf{R}) = [M^+(\mathbf{R})]^*, \quad (A2)$$

$$M_z(\mathbf{R}) = M_0 - \gamma a^*(\mathbf{R})a(\mathbf{R}), \quad (A3)$$

where the single-site variables are related to the \mathbf{k} -dependent spin-wave variables via

$$a(\mathbf{R}) = \sum_{\mathbf{k}} a_{\mathbf{k}} e^{i\mathbf{k}\cdot\mathbf{R}}. \quad (A4)$$

Both \mathbf{k} and \mathbf{R} are 2D vectors in the plane of the thin film. Fourier amplitudes $a_{\mathbf{k}}^*$ and $a_{\mathbf{k}}$ are the classical analogs of magnon creation and annihilation operators. If we were including the finite thickness of the magnetic film, we would need to modify this expansion by use of appropriate orthonormal functions through the film thickness, as in Ref. 11. However, in that work Livesey *et al.* showed that a 2D treatment gives the same result for a 15-nm $\text{Ni}_{81}\text{Fe}_{19}$ film, and this vastly simplifies the mathematics involved.

The classical 2D Holstein-Primakoff transformation has the result that the energy becomes a Hamiltonian for the system in the sense that the torque equation of motion for the magnetization,

$$\frac{\partial \mathbf{M}}{\partial t} = \gamma \mathbf{M} \times \left(-\frac{\delta E}{\delta \mathbf{M}} \right), \quad (A5)$$

is transformed into a Hamiltonian equation of motion in terms of the spin-wave variables, namely

$$\frac{\partial a_{\mathbf{k}}}{\partial t} = -i \frac{\delta \mathcal{H}}{\delta a_{\mathbf{k}}^*}. \quad (A6)$$

The Hamiltonian contains two-, three- and four-wave terms, plus higher order terms that we shall ignore. It has the form

$$\begin{aligned} \mathcal{H} &= \mathcal{H}_{2\text{wave}} + \mathcal{H}_{3\text{wave}} + \mathcal{H}_{4\text{wave}} + \dots \\ &= \sum_{\mathbf{k}} \left[A(\mathbf{k}) a_{\mathbf{k}}^* a_{\mathbf{k}} + \frac{1}{2} B(\mathbf{k}) (a_{\mathbf{k}} a_{-\mathbf{k}} + \text{c.c.}) \right] \\ &\quad + \sum_{1,2,3} \delta(\mathbf{k}_1 - \mathbf{k}_2 - \mathbf{k}_3) [C(\mathbf{k}_3) a_{\mathbf{k}_1}^* a_{\mathbf{k}_2} a_{\mathbf{k}_3} + \text{c.c.}] \\ &\quad + \sum_{1,2,3,4} \delta(\mathbf{k}_1 - \mathbf{k}_2 - \mathbf{k}_3 - \mathbf{k}_4) [F(\mathbf{k}_4) a_{\mathbf{k}_1}^* a_{\mathbf{k}_2} a_{\mathbf{k}_3} a_{\mathbf{k}_4} + \text{c.c.}] \\ &\quad + \sum_{1,2,3,4} \delta(\mathbf{k}_1 + \mathbf{k}_2 - \mathbf{k}_3 - \mathbf{k}_4) G(\mathbf{k}_1, \mathbf{k}_3) a_{\mathbf{k}_1}^* a_{\mathbf{k}_2}^* a_{\mathbf{k}_3} a_{\mathbf{k}_4} \\ &\quad + \dots \end{aligned} \quad (A7)$$

The coefficients are made up of combinations of the physical constants and material parameters and are given by

$$\begin{aligned} A(\mathbf{k}) &= 2\pi\gamma M_0 [P(\mathbf{k}) \cos^2 \psi + 1] + \frac{2\gamma\alpha k^2}{M_0} \\ &\quad + \gamma(H_{\text{bias}} \cos \Psi + H_{\text{pulse}} \sin \Psi) \\ &\quad + \gamma H_{\text{uni}} [3 \cos^2(\Psi - \phi) - 1], \end{aligned} \quad (A8)$$

$$\begin{aligned} B(\mathbf{k}) &= 2\pi\gamma M_0 [P(\mathbf{k})(\sin^2 \psi + 1) - 1] \\ &\quad - \gamma H_{\text{uni}} \sin^2(\Psi - \phi), \end{aligned} \quad (A9)$$

$$\begin{aligned} \frac{C(\mathbf{k}_3)}{\gamma\sqrt{2\gamma M_0}} &= -\frac{\pi}{2} P(\mathbf{k}_3) \sin 2\psi_3 - \frac{5H_{\text{uni}}}{8M_0} \sin 2(\Psi - \phi) \\ &\quad - \frac{1}{8M_0} (H_{\text{bias}} \sin \Psi - H_{\text{pulse}} \cos \Psi), \end{aligned} \quad (A10)$$

$$F(\mathbf{k}_4) = \frac{\pi\gamma^2}{2}[1 - P(k_4)\sin^2\psi_4] + \frac{H_{\text{uni}}\gamma^2}{4M_0}\sin^2(\Psi - \phi), \quad (\text{A11})$$

$$G(\mathbf{k}_1, \mathbf{k}_3) = \pi\gamma^2[4\cos^2\psi_{\mathbf{k}_1-\mathbf{k}_3}P(|\mathbf{k}_1 - \mathbf{k}_3|) + 2\cos^2\psi_1P(k_1) - 2] + \frac{\gamma^2\alpha}{M_0^2}(k_1^2 + k_3^2 - 4\mathbf{k}_1 \cdot \mathbf{k}_3) - \frac{\gamma^2H_{\text{uni}}}{M_0}[3\cos^2(\Psi - \phi) - 1], \quad (\text{A12})$$

where Ψ is the angle between the bias field and the internal magnetic field when the pulse is applied, and ϕ is the angle between the bias field and the easy anisotropy axis. The dipolar function contained in these coefficients is given by

$$P(k) = 1 - \frac{1 - e^{-kL}}{kL}. \quad (\text{A13})$$

The next step is to diagonalize the Hamiltonian [Eq. (A7)] by use of a Bogoliubov transformation from circular to elliptical spin-wave variables b_k^* and b_k ²⁹:

$$b_k = u_k a_k + v_k a_{-k}^*, \quad (\text{A14})$$

where the coefficients of the transformation are given by

$$u_k = \sqrt{\frac{A(\mathbf{k}) + \omega_k}{2\omega_k}}, \quad (\text{A15})$$

$$v_k = \sqrt{\frac{A(\mathbf{k}) - \omega_k}{2\omega_k}}, \quad (\text{A16})$$

and the two-wave coefficient is

$$\omega_k = \sqrt{A^2(\mathbf{k}) - B^2(\mathbf{k})}. \quad (\text{A17})$$

With this second transformation to elliptical spin-wave variables, the Hamiltonian takes the form of Eq. (15).

When three-wave decay of the precession is not allowed in a system, then another quasilinear transformation must be

performed in order to eliminate the direct three-wave part of the spin-wave Hamiltonian and incorporate them to second-order in perturbation theory within the four-wave part of the Hamiltonian.^{29,37} We have such a case here, as discussed in the main text of Sec. III. However, the thin thickness of the film, together with the fact that we excite mainly backward volume magnetostatic spin waves (BVMSWs) or, more precisely, spin waves with \mathbf{k} aligned within an angle of ~ 1 deg from the internal field direction, means that this transformation has very little effect on the four-wave scattering coefficient $V_{\mathbf{k}_1, \mathbf{k}_2, \mathbf{k}_3, \mathbf{k}_4}^{(2)}$ that we are interested in. This is because four-wave scattering made up of two three-wave scattering events is nonresonant for such a thin film with small applied field. We have confirmed numerically that $V_{\mathbf{k}_1, \mathbf{k}_2, \mathbf{k}_3, \mathbf{k}_4}^{(2)}$ is relatively unchanged by the quasilinear transformation (see Fig. 6 of Ref. 11).

The four wave scattering coefficient $V^{(2)}$ is given by direct substitution of the Bogoliubov transformation [Eq. (A14)] into the Hamiltonian [Eq. (A7)] and then grouping together four-wave terms of the form b^*b^*bb . The unsymmetrized coefficient is

$$V_{\text{un}}^{(2)}(\mathbf{k}_1, \mathbf{k}_2, \mathbf{k}_3, \mathbf{k}_4) = G(\mathbf{k}_1, \mathbf{k}_3)u_{\mathbf{k}_1}u_{\mathbf{k}_2}u_{\mathbf{k}_3}u_{\mathbf{k}_4} + G(\mathbf{k}_1, -\mathbf{k}_2)u_{\mathbf{k}_1}v_{\mathbf{k}_2}v_{\mathbf{k}_3}u_{\mathbf{k}_4} + G(-\mathbf{k}_3, -\mathbf{k}_1)v_{\mathbf{k}_1}u_{\mathbf{k}_2}v_{\mathbf{k}_3}u_{\mathbf{k}_4} + G(\mathbf{k}_1, \mathbf{k}_3)u_{\mathbf{k}_1}v_{\mathbf{k}_2}u_{\mathbf{k}_3}v_{\mathbf{k}_4} + G(-\mathbf{k}_4, \mathbf{k}_3)v_{\mathbf{k}_1}u_{\mathbf{k}_2}u_{\mathbf{k}_3}v_{\mathbf{k}_4} + G(-\mathbf{k}_3, -\mathbf{k}_1)v_{\mathbf{k}_1}v_{\mathbf{k}_2}v_{\mathbf{k}_3}v_{\mathbf{k}_4} - 2[2F(\mathbf{k}_4) + F(-\mathbf{k}_2)]u_{\mathbf{k}_1}v_{\mathbf{k}_2}u_{\mathbf{k}_3}u_{\mathbf{k}_4} - 2[F(\mathbf{k}_4) + F(-\mathbf{k}_1) + F(-\mathbf{k}_2)]v_{\mathbf{k}_1}v_{\mathbf{k}_2}v_{\mathbf{k}_3}u_{\mathbf{k}_4}, \quad (\text{A18})$$

but then we force the coefficient to obey the required symmetries by replacing it by the average of all permutations which should be equivalent:

$$V_{\mathbf{k}_1, \mathbf{k}_2, \mathbf{k}_3, \mathbf{k}_4}^{(2)} \rightarrow \frac{1}{8} [V_{\text{un}}^{(2)}(\mathbf{k}_1, \mathbf{k}_2, \mathbf{k}_3, \mathbf{k}_4) + V_{\text{un}}^{(2)}(\mathbf{k}_2, \mathbf{k}_1, \mathbf{k}_3, \mathbf{k}_4) + V_{\text{un}}^{(2)}(\mathbf{k}_1, \mathbf{k}_2, \mathbf{k}_4, \mathbf{k}_3) + V_{\text{un}}^{(2)}(\mathbf{k}_2, \mathbf{k}_1, \mathbf{k}_4, \mathbf{k}_3) + V_{\text{un}}^{(2)}(\mathbf{k}_3, \mathbf{k}_4, \mathbf{k}_1, \mathbf{k}_2) + V_{\text{un}}^{(2)}(\mathbf{k}_4, \mathbf{k}_3, \mathbf{k}_1, \mathbf{k}_2) + V_{\text{un}}^{(2)}(\mathbf{k}_3, \mathbf{k}_4, \mathbf{k}_2, \mathbf{k}_1) + V_{\text{un}}^{(2)}(\mathbf{k}_4, \mathbf{k}_3, \mathbf{k}_2, \mathbf{k}_1)]. \quad (\text{A19})$$

*Work partially supported by US Government, not subject to US Copyright.

[†]livesey@physics.uwa.edu.au; Current address: CSIRO Earth Science and Resource Engineering, Australian Resources Research Centre, 26 Dick Perry Ave, Kensington WA 6151, Australia.

¹W. K. Hiebert, A. Stankiewicz, and M. R. Freeman, *Phys. Rev. Lett.* **79**, 1134 (1997).

²C. H. Back, R. Allenspach, W. Weber, S. S. P. Parkin, D. Weller, E. L. Garwin, and H. C. Siegmann, *Science* **285**, 864 (1999).

³T. J. Silva, C. S. Lee, T. M. Crawford, and C. T. Rogers, *J. Appl. Phys.* **85**, 7849 (1999).

⁴Th. Gerrits, H. A. M. van den Berg, J. Hohlfield, L. Bär, and Th. Rasing, *Nature (London)* **418**, 509 (2002).

⁵T. J. Silva, P. Kabos, and M. R. Pufall, *Appl. Phys. Lett.* **81**, 2205 (2002).

⁶M. Bauer, J. Fassbender, B. Hillebrands, and R. L. Stamps, *Phys. Rev. B* **61**, 3410 (2000).

⁷B. Hillebrands and J. Fassbender, *Nature (London)* **418**, 493 (2002).

⁸R. L. Stamps and B. Hillebrands, *Appl. Phys. Lett.* **75**, 1143 (1999).

⁹A. Yu. Dobin and R. H. Victora, *Phys. Rev. Lett.* **90**, 167203 (2003).

¹⁰A. Yu. Dobin and R. H. Victora, *J. Appl. Phys.* **95**, 7139 (2004).

¹¹K. L. Livesey, M. P. Kostylev, and R. L. Stamps, *Phys. Rev. B* **75**, 174427 (2007).

¹²Th. Gerrits, T. J. Silva, J. P. Nibarger, and Th. Rasing, *J. Appl. Phys.* **96**, 6023 (2004).

¹³Th. Gerrits, T. J. Silva, and Th. Rasing, *Rev. Sci. Instrum.* **77**, 034704 (2006).

¹⁴P. Kabos, A. B. Kos, and T. J. Silva, *J. Appl. Phys.* **87**, 5980 (2000).

¹⁵H. Suhl, *J. Phys. Chem. Solids* **1**, 209 (1957).

¹⁶J. M. Florczak and E. Dan Dahlberg, *J. Appl. Phys.* **67**, 752 (1990).

- ¹⁷Z. J. Yang and M. R. Scheinfein, *J. Appl. Phys.* **74**, 6810 (1993).
- ¹⁸A. Berger and M. R. Pufall, *Appl. Phys. Lett.* **71**, 965 (1997).
- ¹⁹A. Berger and M. R. Pufall, *J. Appl. Phys.* **85**, 4583 (1999).
- ²⁰J. S. Dodge, L. Klein, M. M. Fejer, and A. Kapitulnik, *J. Appl. Phys.* **79**, 6186 (1996).
- ²¹H. F. Ding, S. Putter, H. P. Oepfen, and J. Kirschner, *Phys. Rev. B* **63**, 134425 (2001).
- ²²J.-W. Lee, J. Kim, S.-K. Kim, J.-R. Jeong, and S.-Ch. Shin, *Phys. Rev. B* **65**, 144437 (2002).
- ²³S. Vischnovsky, *Czech. J. Phys. B* **36**, 1424 (1986).
- ²⁴J. Hamrle, S. Blomeier, O. Gaier, B. Hillebrands, H. Schneider, K. Postava, and C. Felser, *J. Phys. D* **40**, 1563 (2007).
- ²⁵M. Buchmeier, R. Schreiber, D. E. Burgler, and C. M. Schneider, *Phys. Rev. B* **79**, 064402 (2009).
- ²⁶K. Postava, J. F. Bobo, M. D. Ortega, B. Raquet, H. Jaffres, E. Snoek, M. Goiran, A. R. Fert, J. P. Redoules, J. Pistora, and J. C. Ousset, *J. Magn. Magn. Mater.* **163**, 8 (1996).
- ²⁷K. Postava, D. Hrabovsky, J. Pistora, A. R. Fert, S. Vischnovsky, and T. Yamaguchi, *J. Appl. Phys.* **91**, 7293 (2002).
- ²⁸B. A. Kalinikos, *Sov. Phys. J.* **24**, 719 (1981).
- ²⁹V. S. L'vov, *Wave Turbulence Under Parametric Excitation* (Springer, Berlin, 1994).
- ³⁰A. Slavin and V. Tiberkevich, *Phys. Rev. Lett.* **95**, 237201 (2005).
- ³¹E. Schlömann, *Phys. Rev.* **116**, 828 (1959).
- ³²V. E. Zakharov, V. S. L'vov, and S. S. Starobinets, *Sov. Phys. Usp.* **17**, 896 (1975); *Usp. Fiz. Nauk* **114**, 609 (1974).
- ³³A. D. Boardman and S. A. Nikitov, *Phys. Rev. B* **38**, 11444 (1988).
- ³⁴B. Heinrich, J. F. Cochran, and R. Hasegawa, *J. Appl. Phys.* **57**, 3690 (1985).
- ³⁵R. Arias and D. L. Mills, *Phys. Rev. B* **60**, 7395 (1999).
- ³⁶S. S. Kalarickal, P. Krivosik, M. Wu, C. Patton, M. L. Schneider, P. Kabos, T. J. Silva, and J. P. Nibarger, *J. Appl. Phys.* **99**, 093909 (2006).
- ³⁷V. P. Krasitskii, *Sov. Phys. JETP* **71**, 921 (1990) [*Zh. Eksp. Teor. Fiz.* **98**, 1644 (1990)].